

# Grating-Structured Freestanding Triboelectric Nanogenerator for Self-Powered Acceleration Sensing in Real Time

Yufeng Liu, Ding Li,\* Yu Hou, and Zhong Lin Wang\*

Acceleration sensors have wide applications in earthquake warning, human motion recognition, vehicle restraint system, etc. However, the existing commercial acceleration sensors have some limitations on needing an external power supply, high fabrication cost, and small signal when self-powered. Here a grating-structured freestanding triboelectric nanogenerator (GF-TENG) capable of sensing displacements, velocities, and accelerations in real-time is presented with self-powered, low cost, and sufficiently large signal. The slider with grating-structured electrodes of GF-TENG sliding over the stator with another grating-structured electrode generates the periodic open-circuit voltage due to electrostatic induction. By recognizing the shape of open-circuit voltage, it could sense the acceleration in real time even at scales down to hundred microns through systematic optimization of simulations and experiments. Furthermore, the acceleration sensing range could be expanded to the desired ranges, such as 5.0 to 45.0  $\text{m s}^{-2}$ , by assembling springs and GF-TENG into a grating-structured TENG-based acceleration sensor (GTAS). Moreover, GTAS is demonstrated to sense the vehicle motion and be a part of the vehicle restraint system on a model car. This work reports a new self-powered acceleration sensor with sufficiently large outputs for real-time motion sensing and collision detection, which could be further applied for robotics and human motion recognition.

## 1. Introduction

Acceleration sensors have a wide range of applications in earthquake early warning, human motion recognition, sleep monitoring, vibration test, and vehicle monitoring.<sup>[1–5]</sup> The acceleration sensor also plays an important role in the vehicle restraint system, as it detects the collision direction and position and switches on the airbag to protect the passengers. Generally, the existing commercial acceleration sensors are mainly divided into categories of capacitive, piezoresistive, and piezoelectric according to their physical principle.<sup>[6–8]</sup> However, these existing commercial sensors have their own limitations. Capacitive and piezoresistive acceleration sensors require an external power supply to operate, which might hinder their applications in Internet of Things, and consume extra energy for battery replacements. Piezoelectric acceleration sensor is self-powered with small output signal ( $<0.2$  V after amplifier when acceleration is 6 g, for example), which might make it susceptible to environmental noise. Therefore, a self-powered acceleration sensor with sufficiently large

outputs (in the range of 0–10 V without an amplifier circuit) is desired.

In 2012, triboelectric nanogenerator (TENG) was invented by Wang's research group, with advances of cost-effective, highly efficient, and easy-fabricated.<sup>[9]</sup> It has been used to harvest the ambient energy like wind,<sup>[10–12]</sup> rain,<sup>[13,14]</sup> ocean wave,<sup>[15,16]</sup> human motion,<sup>[17,18]</sup> vibration,<sup>[19]</sup> and other type of energy.<sup>[20–22]</sup> More importantly, benefitting from its' unique response to external excitations, the TENG has been made into a variety of self-powered sensors, including tactile,<sup>[23–26]</sup> acoustics,<sup>[27,28]</sup> vehicle,<sup>[29]</sup> displacement,<sup>[30–32]</sup> and angle sensors.<sup>[33]</sup> TENG can also be used to make acceleration sensors, for example: Pang et al. reported a 3D acceleration sensor that can detect acceleration from 13 to 40  $\text{m s}^{-2}$ ,<sup>[34]</sup> Wu et al. made a 2D acceleration sensor with the detection range from 6 to 50  $\text{m s}^{-2}$ ,<sup>[35]</sup> Zhang et al. demonstrated a 3D sensor based on TENG that achieved the smallest volume and the detection range from close 0 to 100  $\text{m s}^{-2}$ . And its response time was 7 ms when acceleration was 100  $\text{m s}^{-2}$ .<sup>[36]</sup> The size of these TENG-based acceleration sensors is gradually decreasing and the measurement range is getting larger. However, the above acceleration sensors

Y. Liu, D. Li, Y. Hou, Z. L. Wang  
Center on Nanoenergy Research  
School of Physical Science and Technology  
Guangxi University  
Nanning, Guangxi 530004, P. R. China  
E-mail: liding@binn.cas.cn

Y. Liu, D. Li, Y. Hou, Z. L. Wang  
Beijing Key Laboratory of Micro-Nano Energy and Sensor  
Beijing Institute of Nanoenergy and Nanosystems  
Chinese Academy of Sciences  
Beijing 101400, P. R. China

D. Li, Z. L. Wang  
School of Nanoscience and Technology  
University of Chinese Academy of Sciences  
Beijing 100049, P. R. China

Z. L. Wang  
School of Material Science and Engineering  
Georgia Institute of Technology  
Atlanta, GA 30332-0234, USA  
E-mail: zhong.wang@mse.gatech.edu

 The ORCID identification number(s) for the author(s) of this article can be found under <https://doi.org/10.1002/admt.202200746>.

DOI: 10.1002/admt.202200746

cannot sense the changes of acceleration over time in real-time. Although Zhang's acceleration sensor was small in size, its signal output was also small (<0.3 V) in plane. In real applications, for a side impact sensing system of a vehicle, it takes 6–13 ms to determine the crash condition while for a frontal impact sensing system takes 15–25 ms.<sup>[37]</sup> The response time of the TENG-based self-powered acceleration sensor also needs to be reduced to meet these requirements. Therefore, it is necessary to develop a new acceleration sensor based on TENG with small size, large measuring range, and fast response time.

Here, we report a self-powered acceleration sensor, based on grating-structured freestanding TENG (GF-TENG). The GF-TENG can sense the displacement with a minimum resolution of 0.4 mm. And it can also sense the velocity and the acceleration in real-time. The GF-TENG could be further assembled with springs to form a GF-TENG based acceleration sensor (GTAS) capable of sensing desired acceleration range with small size, fast response time, and no amplifier circuit requirement. The GTAS can achieve about 5.88 ms response time when the acceleration is 45 m s<sup>-2</sup>. And the GTAS exhibits the potential of application in the vehicle for monitoring the motion state and switching on vehicle restraint system to protect the passenger from the injury.

## 2. Results and Discussion

### 2.1. Structure and Working Principle of GTAS

The structure and sensing mechanism of the GTAS are depicted in **Figure 1** with possible applications (Figure 1a). When GTAS is mounted in the car, it can not only detect the car's running state, but also detect the collision force and direction. The self-power signal of GTAS could feedback to open up the vehicle restraint system promptly to protect people from injury. The basic parameters of GTAS are shown in Figure 1b. The size of GTAS is 3.19 × 2.35 × 1.74 cm<sup>3</sup>, and its weight is about 15.81 g. The detailed structure of GTAS with exploded view is shown in Figure 1c. The four acrylic plates are connected to form the frame of the device through the tenon and mortise structure (Figure S2b, Supporting Information). The length and width of acrylic plates can be changed to control the size of the device. The distance between the slider and the stator can be adjusted by changing the locations of the tenon and mortise. Four groups of bolt and nut ensure the stator is fixed on the bottom acrylic plate. The stator is composed of the interdigital electrode printed circuit board (PCB) and fluorinated ethylene propylene (FEP) film. The two sets of electrodes of interdigital electrode PCB are illustrated in Figure 1c. The FEP film is attached to the interdigital electrode PCB to improve the electric output, which could be enhanced by the nanorod structures created on the FEP film surface by inductive coupling plasma (ICP). The SEM image of nanorod structures on FEP surface can be found in Figure S1 (Supporting Information). The slider consists of a PCB and a steel mass. The PCB beneath the steel mass, we name it as the freestanding PCB, contains a set of parallel electrodes, which could be used as a freestanding electrode in further TENG fabrication. It is glued by double-sided tape beneath the steel mass. The steel mass is center drilled

along a ceramic shaft, and the ceramic shaft is positioned by two concentric bearings, which is embedded in side acrylic plates. Along the two ends of the ceramic shaft, two identical springs are first attached to the thin acrylic gaskets by glue, and then the acrylic gaskets are fixed to the side acrylic plates by hot melt adhesive. Above all, the core part of GTAS is the grating-structured freestanding TENG (GF-TENG) composing of the stator and the PCB beneath the steel mass, which are colored parts in Figure 1c.

The acceleration direction recognition principle of GTAS is depicted in Figure 1d, electrodes A connect with the steel mass by thin copper wire, electrodes B connect with the external circuit, the steel mass and the spring are both conductors. As shown in Figure 1d-i, when the steel mass slides to the left, the steel mass and the left spring will connect. And the voltage signal will appear in the one channel. It shows the acceleration direction is to the right. The same principle will apply when the steel mass slides to the right, and the voltage signal will appear in another channel, showing the acceleration direction is to the left (Figure 1d-ii). Therefore, the direction of acceleration can be distinguished through this special connection design.

The amplitude of acceleration could be determined by GTAS through the open-circuit voltage signals from the GF-TENG. And the mechanism of the GF-TENG is depicted in Figure 1e. FEP film and freestanding electrode play the role of electrification layer. As FEP is more electronegative than copper, the FEP surface will gain electrons and be negatively charged while the copper of freestanding electrode will be positively charged after contact electrification between two surfaces.<sup>[38]</sup> According to the charge conservation law, the charge density on the copper is three times as much as the FEP film as the friction area of FEP film is the triple of the one of the copper. In the initial state, the freestanding electrode is fully overlapping with electrode A (Figure 1e-i), electrodes A and B carry the same amounts of induced charges, but their polarity are opposite. When the freestanding electrode slides rightward, the free electrons flow from electrode A to B via an external circuit due to electrostatic induction (Figure 1e-ii). Then the electrons will continue flowing from electrode A to B, when the freestanding electrode further slides towards electrode B. The charge distribution will be opposite with the initial state when freestanding electrode fully overlapping with electrode B (Figure 1e-iii). The same would apply to the situation when the freestanding electrode slides from B to A (Figure 1e-iv,vi).

To describe the charge transfer quantitatively, a simplified parallel-plate capacitor model is proposed, which is based on the assumption that the thickness of FEP film is far smaller than its' width and length.<sup>[39]</sup> Based on this model, the variation trends of TENG's short-circuit charge ( $Q_{sc}$ ) and open-circuit voltage ( $V_{oc}$ ) can be described as:<sup>[33]</sup>

$$Q_{sc}(x) = -\frac{\sigma_o(x) \cdot S}{1 + \frac{w}{w-x}} - \frac{3 \cdot \sigma S}{2} (0 \leq x \leq w) \quad (1)$$

$$Q_{sc}(x) = \frac{\sigma_o(x) \cdot S}{1 + \frac{w}{x-w}} - \frac{3 \cdot \sigma S}{2} (w < x \leq 2w) \quad (2)$$

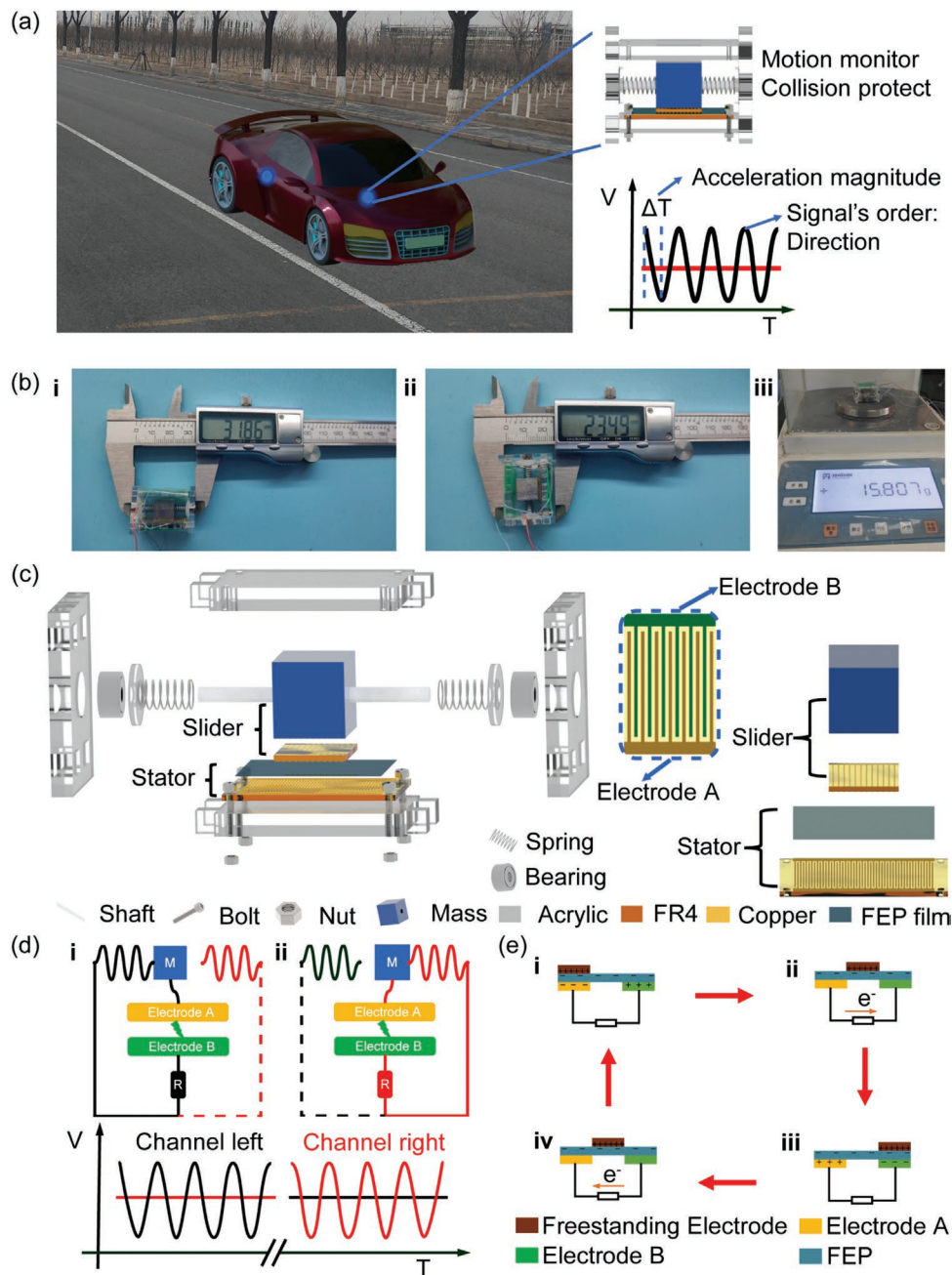


**Figure 1.** The working principle, structure of GTAS with application demonstration. a) GTAS's application demonstration in vehicle motion detection and a part of vehicle restraint system. b) Optical images of the GTAS in i) the length, ii) the width, and iii) the weight. c) Exploded view of GTAS. d) The working mechanism of GTAS recognizing the direction of acceleration. e) The working principle of the GF-TENG, which is the core part of GTAS.

$$V_{oc}(x) = \frac{Q_{sc}(x)}{C} \quad (3)$$

where  $S$  represents the freestanding electrodes area,  $\sigma$  is the charge density value of FEP film surface,  $\sigma_0(x)$  is the charge density of overlapped area on freestanding electrodes,  $w$  is the width of a single electrode unit,  $x$  is the distance of the freestanding electrodes away from the initial state,  $C$  is the capacitance between electrodes A and B.

## 2.2. Optimization of GF-TENG

Figure 2a shows the finite element analysis result (COMSOL Multiphysics). Electrodes A and B are marked in the graph. The electrodes of each group are connected, so the potential of electrodes in the same group is identical. The electric potential distribution between the two groups of electrodes changes with the freestanding electrode's movement. In order to study how the open-circuit voltage changes with the distance of the

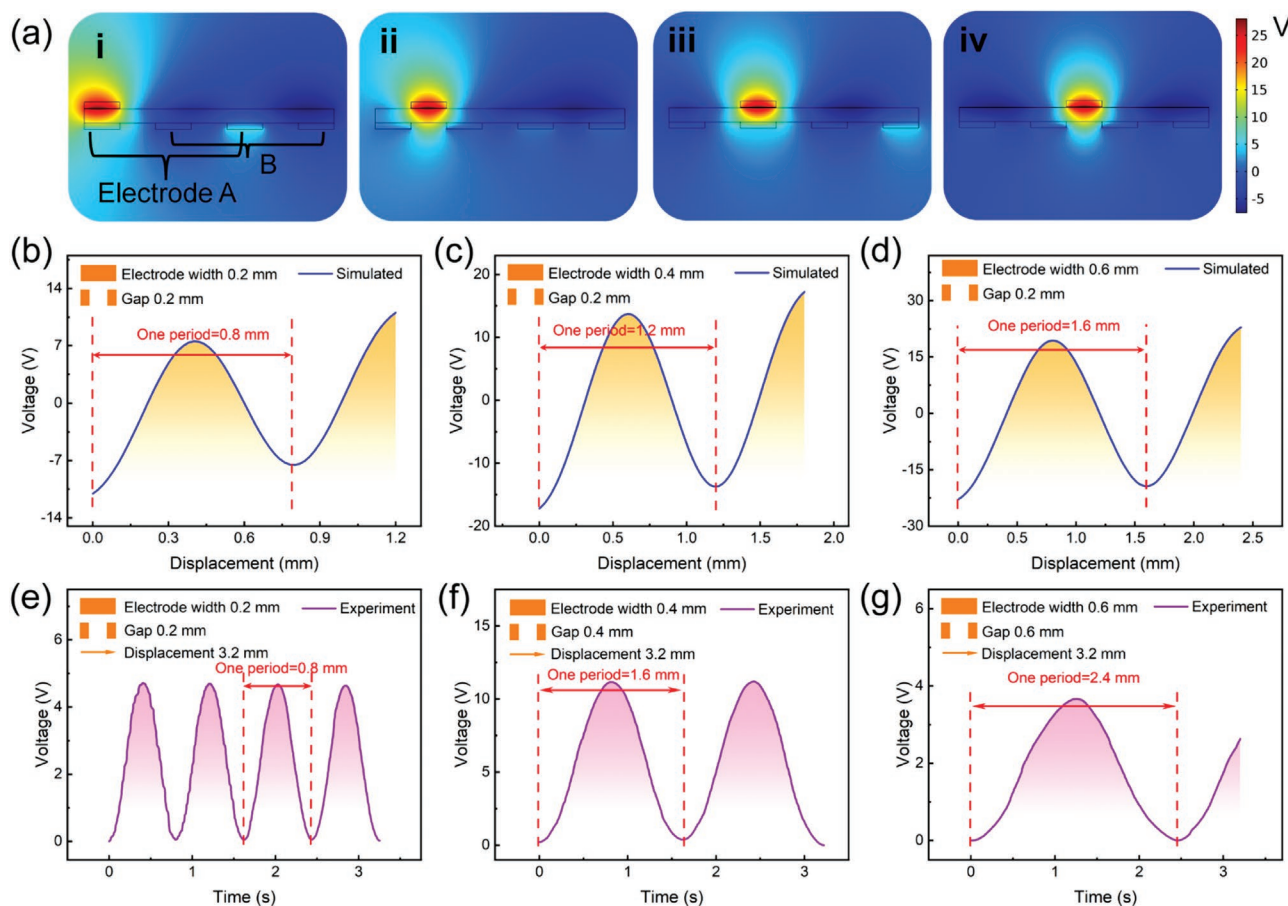


**Figure 2.** The simulation and experimental results of GF-TENG. a) Potential distribution of GF-TENG simulated with COMSOL. b–d) Simulated open-circuit voltage for incremental electrode width: 0.2 mm; 0.4 mm; 0.6 mm. e–g) The open-circuit voltage of GF-TENG with different electrode widths in the experiment for the ratio of electrode width to gap of 1:1.

freestanding electrode away from the initial state, we plot the open-circuit voltage that is the potential of electrode group A minus the potential of electrode group B (Figure 2b–d). In these simulations, we keep the gap between electrodes at 0.2 mm and set up a gradually increase electrode width, which is 0.2, 0.4, and 0.6 mm. And more simulations of the electric potential distribution for the electrode width of 0.4 mm and 0.6 mm can be found in Figure S3 (Supporting Information). Although the waveforms of open-circuit voltage are similar, the periods of the open-circuit voltage correspond to different displacements of freestanding electrode. As the electrode width increases, the valley-to-valley distance of the waveform in one period represents larger displacement. Besides the electrode width, the gap between electrodes would also influence the period of open-circuit voltage. The detailed results of the gap variations are supplied in Figure S4 (Supporting Information). These results are consistent with Equation 3. One period of the open-circuit voltage represents the displacement that is twice of the total distance of electrode width plus gap. By just counting the number of periods, we could obtain the displacement of the freestanding electrode.

To verify the simulation results, the experimental results of open-circuit voltage of three GF-TENG with different electrode widths and gaps are shown in Figure 2e–g with images of fab-

ricated GF-TENGs in Figure S2a (Supporting Information). Three GF-TENG share the same the electrode width to the gap ratio at 1:1, but change the electrode width at 0.2, 0.4, and 0.6 mm, respectively. When the freestanding PCB moves at the speed of  $1 \text{ mm s}^{-1}$  for the same amount of displacement, the open-circuit voltage of TENGs shows different waveforms. The smaller the electrode width is, the more peaks there are. We calculate the period of these TENG's open-circuit voltage, and find out that the period is proportional to the sum of the electrode width and the gap. In order to make the device size smaller, the optimized electrode width and the gap are both 0.2 mm.

### 2.3. Performance of GF-TENG

Using the above-optimized parameters, the real-time sensing abilities of the GF-TENG to the displacement, the velocity, and the acceleration are demonstrated. The GF-TENG is tested by a linear motor and a Keithley electrometer system as the schematic diagram shown in Figure 3a. The optical images of the core parts of TENG, the freestanding PCB, and the interdigital electrode PCB, are also shown in Figure 3a. The slider is stuck to the linear motor to make sure that the slider will move strictly together with it, and the stator is fixed in parallel with

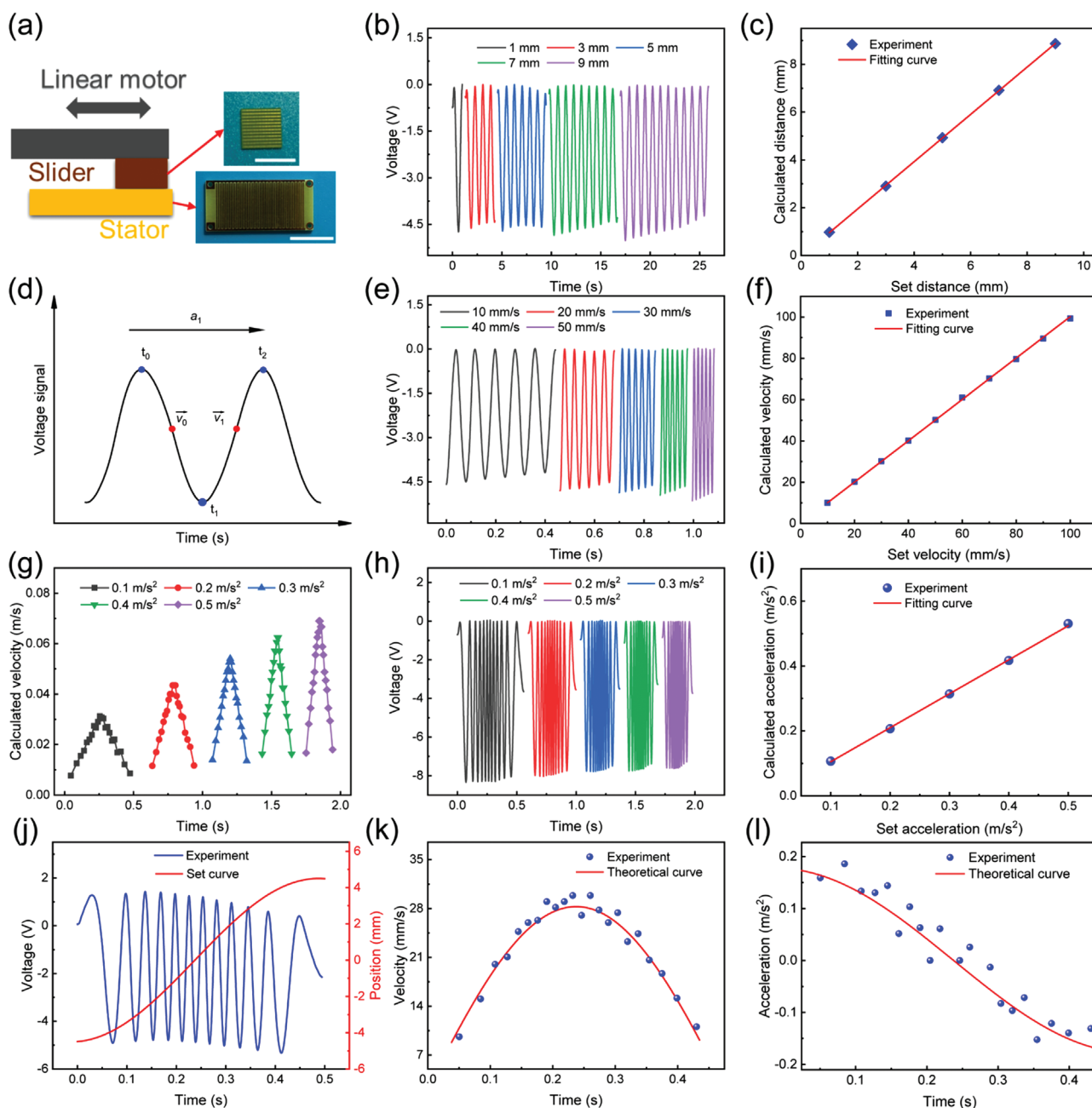


**Figure 3.** The principle and experimental results of GF-TENG capable of sensing displacements, velocities, and accelerations in real time. a) Schematic diagram of GF-TENG motion test and optical images of freestanding PCB and interdigital electrode PCB, scale bar is 1 cm. b) The open-circuit voltage of GF-TENG with the slider moving different distances at the same speed and c) comparing the theoretical value with experimental value. d) Schematic diagram of the method of real-time sensing is based on the recognition of the shape of voltage signals by counting the periods of the open-circuit voltage signal, the time interval between each half-period and the trend of the time interval. e) The open-circuit voltage signals of GF-TENG with the slider moving the same distance at different velocities and f) comparing the experimental values with the theoretical values. g) The real-time velocity during the movement of the slider in the GF-TENG with different uniform accelerations, which are obtained from h) the open-circuit voltage signal. i) The calculated acceleration, derivate from the velocity, is in comparison with the theoretical acceleration. j) The open-circuit voltage signal and theoretical curve when the slider in GF-TENG moves with a sinusoidal curve of position over time. k) The velocity point and theoretical curve during the motion over time, and l) the acceleration value and theoretical curve during the motion over time.

the slider. Figure 3b shows the open-circuit voltage when the slider moves for different distances with the same velocity. As the moving distance increases, the number of periods of the open-circuit voltage will increase linearly with the moving dis-

tance. As every half-period represents the distance of 0.4 mm, we can calculate the displacement of the slider together with the direction recognition principle described in Figure 1d. Figure 3c shows the calculated distance compared with the set

distance, showing they are in good agreement. Figure 3d shows the method we calculate the velocity and the acceleration. Since the peak and valley time point ( $t_0$ ,  $t_1$ ) are easy to get and half-period represents 0.4 mm, we can divide the absolute value of the displacement by time to get the absolute value of the velocities in each half-period. And we can further obtain the acceleration by calculating the changes of the velocities in the whole period. Based on this method, Figure 3e,f shows the calculated absolute value of the velocities compared with the set value and the corresponding open-circuit voltage when the slider moves at different velocities with the same distance of 4.4 mm. As the moving velocity increases, the period of the open-circuit voltage will decrease accordingly.

Based on the real-time sensing abilities of the displacement and the velocity of the GF-TENG, the acceleration can also be obtained by the GF-TENG. Figure 3h exhibits the open-circuit voltage with different accelerations within the moving distance of 9 mm. The slider experiences an acceleration for the first half movement and a deceleration at the same level for the last half movement. The average velocity for each half-period is calculated over the entire movement, which is shown in Figure 3g. The accelerations are obtained by the derivative of the velocities, which is linear with the set value as in Figure 3i. Two more accelerated motions of the slider are also sensed with the GF-TENG, including motions of the accelerated–uniform–decelerated and the accelerated–decelerated at different levels, which is shown in Figure S5 (Supporting Information). There-

fore, this is the first method that the accelerations can be well sensed by the GF-TENG.

The GF-TENG can also be used to sense the time-varying acceleration in real-time. As an example in the experiment, the linear motor is set to move as the position versus time in a way of the sinusoidal curve, where the position of the slider and the open-circuit voltage are shown in Figure 3j. The velocity obtained by GF-TENG sensing is in good agreement with the theoretical velocity curve from the set position versus time curve (Figure 3k). And the acceleration is obtained by differentiating the velocity of the slider, which is shown in Figure 3l. The calculated acceleration points could reflect the time-varying acceleration in real-time and are also in good agreement with the theoretical velocity curve from the set position versus time curve. Although the output of GF-TENG decreases as the relative humidity increases, the period of its open-circuit voltage remains unchanged and does not affect its sensing capability (Figure S6, Supporting Information).

#### 2.4. Performance of GTAS

When we assemble GF-TENG into GTAS, the measuring range of GTAS would be expanded by adjusting the spring constant of springs and the mass of the steel mass. Under the spring constant of  $0.13 \text{ N mm}^{-1}$  and the steel mass of 7.5 g, the open-circuit voltage of GTAS is shown in Figure 4a when the accelerations are

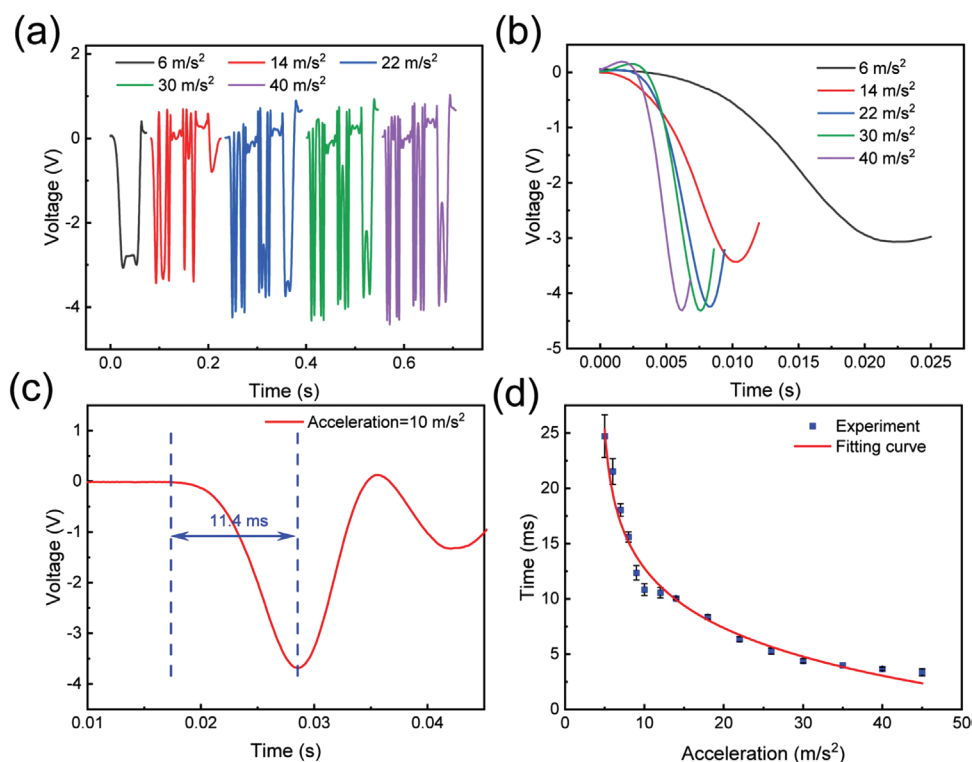


**Figure 4.** The acceleration sensing range could be expanded to the desired ranges, such as 5.0 to 45.0  $\text{m s}^{-2}$ , by assembling springs and GF-TENG into GTAS. a) The open-circuit voltage of GTAS at different accelerations. b) The enlarged view of the open-circuit voltage of GTAS goes from emergence to the first valley at different accelerations. c) The response time calculated from the open-circuit voltage of GTAS at an acceleration of  $10 \text{ m s}^{-2}$ . d) The summary relationship and logarithmic fit between the response time and acceleration. Data summarized as the mean with error bars representing the 95% confidence interval. Sample size ( $n$ ) for each measurement is 5.

6, 14, 22, 30, and 40  $\text{m s}^{-2}$ , respectively. The open-circuit voltage can be divided into the process of compression of the spring by the slider and recovery of the spring, and the compression process is important for sensing acceleration in another way. For each individual acceleration, the time taken for the slider within the GTAS to slide from the initial position to the position where the open-circuit voltage at the valley is unique. We define this time interval as response time and the open-circuit voltage at the same start time for different accelerations is shown in Figure 4b. For example, at 10  $\text{m s}^{-2}$ , the response time of GTAS is 11.4 ms, and its enlarged view is shown in Figure 4c. The logarithmic relation between the response time and the more acceleration sensing results together with the spring on the right side is demonstrated in Figure 4d. As long as the response time is known, we could easily obtain the acceleration by this relationship. This is the second method that the GTAS could provide the acceleration. As shown in Figure S7 (Supporting Information), the acceleration sensing results together with the spring on the left side

are similar to the one on the right side. The stability of the GTAS is also tested (Figure S8, Supporting Information). Therefore, we successfully expand the measurement range of GTAS to the range of 5 to 45  $\text{m s}^{-2}$ . We can also extend the detection range by adjusting the spring constant of springs (Figure S9, Supporting Information).

## 2.5. Demonstration of GTAS

The potential application of GTAS on car as acceleration sense is proved by assembling GTAS to a model car. As shown in Figure 5a-i, the acceleration sensor is fixed upon the model car by double-sided tape, and the acceleration sensor is horizontal and parallel to the model car. The user interface of the program which is written by LABVIEW has a signal display area and a result display area (Figure 5a-ii). The generated voltage signal is displayed on the screen. The red line represents the channel

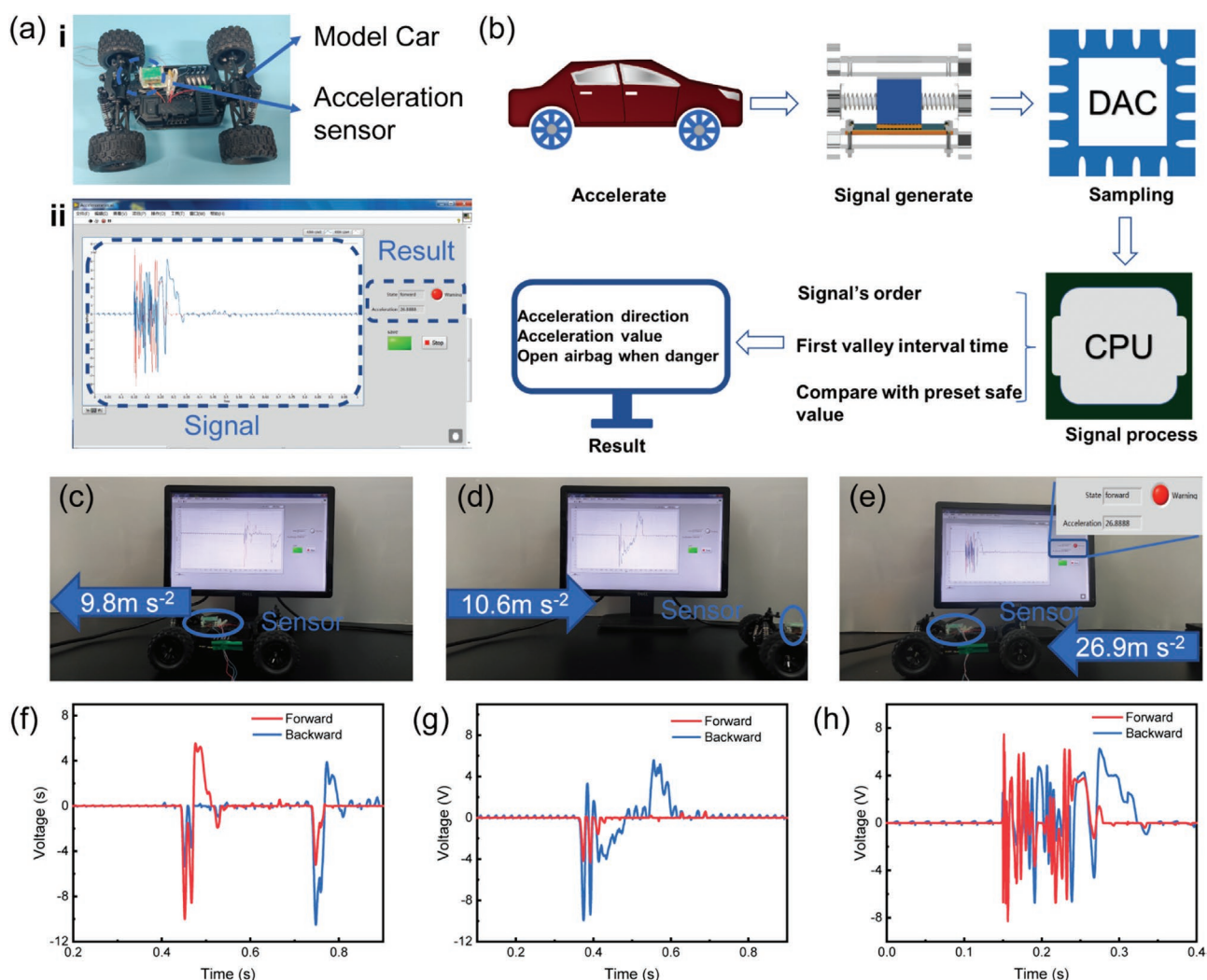


**Figure 5.** The potential application of GTAS on car as acceleration sense on a model car. a) The assembly and software used in the experiments: (i) optical image of the GTAS installed on the model car; (ii) user interface of the program. b) The schematic diagram of the process of sensing the magnitude and direction of acceleration by GTAS. The optical images of the model car as it accelerates forward at c) 9.8  $\text{m s}^{-2}$ , accelerates backward at d) 10.6  $\text{m s}^{-2}$ , and hit by e) a heavy object with f–h) the voltage signal, respectively.

that the slider connects with the spring at the right side and the blue one is at the left side. Figure 5b shows a schematic of the process by which the acceleration sensor identifies the magnitude and direction of acceleration. When the model car accelerates, the multi-channel data acquisition card (DAC) collects the signals generated by the GTAS. The pulsed voltage signals will be processed by the central processing unit (CPU) and the direction can be identified by comparing which channel's signal occurs first, and the magnitude of the acceleration will be distinguished by the response time. Figure 5c,f shows the voltage signal that is red occurred first before blue one, indicating the acceleration direction is forward, and the value is  $9.8 \text{ m s}^{-2}$ . In Figure 5d–g, the blue line appears before the red line, indicating the backward acceleration of the model car with a magnitude of  $10.6 \text{ m s}^{-2}$  (Video S1, Supporting Information). Collision detection is important for vehicles because of the need to quickly determine whether to activate the appropriate protective measures to safeguard passengers in the event of a collision. Therefore, we use GTAS to detect and warn of collisions, as shown in Figure 5e. When a collision happens, the GTAS responds quickly and the warning button lights up. Figure 5h shows that the acceleration direction is forward with a value of  $26.9 \text{ m s}^{-2}$ . The long duration of the voltage signal indicates that the force caused by the external collision is high causing the slider to slide back and forth (Video S2, Supporting Information). Overall, the above experiments demonstrate the potential of GTAS in practical applications.

### 3. Conclusion

In summary, we developed a self-powered acceleration sensor based on a grating-structured TENG capable of sensing the displacement, velocity, and acceleration in real-time. GF-TENG consists of a slider containing one set of parallel electrodes and a stator with two sets of parallel electrodes, and the slider sliding generates the periodic open-circuit voltage due to electrostatic induction. The sensing principle is based on the recognition of the shape of the open-circuit voltage by counting the periods of the open-circuit voltage signal, the time interval between each half-period and the trend of the time interval. It avoids the sensing principle based on the magnitude of the voltage of previous TENGs, which is easily affected by environmental changes, such as humidity, temperature, and environmental disturbance. Through systematic simulation and experiment of electrode width and gap, the optimized values for GF-TENG are found. It could sense displacements, velocities, and accelerations in real-time even at scales down to hundred microns. Furthermore, the acceleration sensing range could be expanded to the desired ranges by assembling springs and GF-TENG into a GTAS. The GTAS identifies the direction of acceleration by using springs and a steel mass as a switch for the open-circuit voltage signal in both directions. Moreover, we demonstrate the ability of GTAS to be used to sense the motion of vehicle and its application in the vehicle restraint system on a model car. In future, the GF-TENG's sensing precision and resolution could be further improved by PCB processing capability and accuracy. And the GTAS could be made into a 3D acceleration sensor and have more application fields, such as robotics and human motion recognition.

### 4. Experimental Section

**GTAS Fabrication:** Four 3 mm thick and two 1 mm thick acrylic boards were processed using a laser cutter (Universal Laser System, PLS6.75) to form the tenon and mortise structure and the spring gaskets (Figure S2b, Supporting Information). The ceramic shaft's diameter is 2 mm, and bearings' inner diameter is 2 mm with an outer diameter of 6 mm. The center of the steel mass was drilled with a hole of about 2 mm. The springs were fabricated with 0.25 mm wire diameter, 3.93 mm outer diameter and 7.0 mm in length. The detailed procedure of PCB manufacturing is: The substrate chosen for the freestanding PCB and interdigital electrode PCB is FR4 epoxy glass with a thickness of 0.8 mm. To transfer the copper pattern onto this substrate, a 35  $\mu\text{m}$  thick full copper sheet was first covered on the FR4 substrate by a cold rolling process, and then a sensitive drying layer was laminated on top of the copper sheet. Afterward, the sensitive layer was exposed to patterned UV light by means of a photographic tool, and the unexposed portion of the layer was removed by the developer. Excess copper was removed from the patterned copper by etching with a ferric chloride solution before stripping the dry film layer.

**Electrical Measurement:** The open-circuit voltage was measured with a Keithley 6514 electrometer system, and the motion of the slider and GTAS is controlled with a linear motor (LinMot B01-37 $\times$ 166/360). In the model car application experiment, a multi-channel data acquisition card (DAC, PXIe-4300, National Instruments) was used to collect the voltage signal of the acceleration sensor.

**Statistical Analysis:** All response time was processed by OriginPro 2022 (Learning Edition), with a statistical significance level  $P \leq 0.05$ , with data summarized as the mean with error bars representing the 95% confidence interval. Sample size ( $n$ ) is shown in the caption of each figure.

### Supporting Information

Supporting Information is available from the Wiley Online Library or from the author.

### Acknowledgements

This research was supported by the National Key R&D Project from the Ministry of Science and Technology of the People's Republic of China (2021YFA1201601) and the National Natural Science Foundation of China (Grant Nos. 52002028, 52192610).

### Conflict of Interest

The authors declare no conflict of interest.

### Data Availability Statement

The data that support the findings of this study are available from the corresponding author upon reasonable request.

### Keywords

acceleration sensor, grating-structured electrodes, self-powered, triboelectric nanogenerator, vehicle restraint system

Received: May 6, 2022

Revised: June 26, 2022

Published online:

- [1] A. Zollo, O. Amoroso, M. Lancieri, Y.-M. Wu, H. Kanamori, *Geophys. J. Int.* **2010**, *183*, 963.
- [2] J. P. Varkey, D. Pompili, T. A. Walls, *Pers. Ubiquit. Comput.* **2012**, *16*, 897.
- [3] S. E. Jones, V. T. van Hees, D. R. Mazzotti, P. Marques-Vidal, S. Sabia, A. van der Spek, H. S. Dashti, J. Engmann, D. Kocevskaja, J. Tyrrell, R. N. Beaumont, M. Hillsdon, K. S. Ruth, M. A. Tuke, H. Yaghootkar, S. A. Sharp, Y. Ji, J. W. Harrison, R. M. Freathy, A. Murray, A. I. Luik, N. Amin, J. M. Lane, R. Saxena, M. K. Rutter, H. Tiemeier, Z. Kutalik, M. Kumari, T. M. Frayling, M. N. Weedon, et al., *Nat. Commun.* **2019**, *10*, 1585.
- [4] A. Vallan, M. L. Casalicchio, G. Perrone, *IEEE Trans. Instrum. Meas.* **2010**, *59*, 1389.
- [5] W. Zhao, J. Yin, X. Wang, J. Hu, B. Qi, T. Runge, *Sensors* **2019**, *19*, 4108.
- [6] H. Zhang, X. Wei, Y. Ding, Z. Jiang, J. Ren, *Sens. Actuators, A* **2019**, *296*, 79.
- [7] P. Dong, X. Li, H. Yang, H. Bao, W. Zhou, S. Li, S. Feng, *Sens. Actuators, A* **2008**, *141*, 339.
- [8] Z. Shen, C. Y. Tan, K. Yao, L. Zhang, Y. F. Chen, *Sens. Actuators, A* **2016**, *241*, 113.
- [9] F. R. Fan, Z. Q. Tian, Z. L. Wang, *Nano Energy* **2012**, *1*, 328.
- [10] Y. Feng, L. Zhang, Y. Zheng, D. Wang, F. Zhou, W. Liu, *Nano Energy* **2019**, *55*, 260.
- [11] S. Wang, X. Wang, Z. L. Wang, Y. Yang, *ACS Nano* **2016**, *10*, 5696.
- [12] S. Yong, J. Wang, L. Yang, H. Wang, H. Luo, R. Liao, Z. L. Wang, *Adv. Energy Mater.* **2021**, *11*, 2101194.
- [13] X. Liu, A. Yu, A. Qin, J. Zhai, *Adv. Mater. Technol.* **2019**, *4*, 1900608.
- [14] W. Xu, H. Zheng, Y. Liu, X. Zhou, C. Zhang, Y. Song, X. Deng, M. Leung, Z. Yang, R. X. Xu, Z. L. Wang, X. C. Zeng, Z. Wang, *Nature* **2020**, *578*, 392.
- [15] X. Liang, T. Jiang, G. Liu, Y. Feng, C. Zhang, Z. L. Wang, *Energy Environ. Sci.* **2020**, *13*, 277.
- [16] C. Zhang, L. He, L. Zhou, O. Yang, W. Yuan, X. Wei, Y. Liu, L. Lu, J. Wang, Z. L. Wang, *Joule* **2021**, *5*, 1613.
- [17] X. Gang, Z. H. Guo, Z. Cong, J. Wang, C. Chang, C. Pan, X. Pu, Z. L. Wang, *ACS Appl. Mater. Interfaces* **2021**, *13*, 20145.
- [18] Y. Xi, J. Hua, Y. Shi, *Nano Energy* **2020**, *69*, 104390.
- [19] L. Wang, T. He, Z. Zhang, L. Zhao, C. Lee, G. Luo, Q. Mao, P. Yang, Q. Lin, X. Li, R. Maeda, Z. Jiang, *Nano Energy* **2021**, *80*, 105555.
- [20] L. Liu, X. Guo, W. Liu, C. Lee, *Nanomaterials* **2021**, *11*, 2975.
- [21] X. Guo, L. Liu, Z. Zhang, S. Gao, T. He, Q. Shi, C. Lee, *J. Micromech. Microeng.* **2021**, *31*, 093002.
- [22] L. Liu, X. Guo, C. Lee, *Nano Energy* **2021**, *88*, 106304.
- [23] Y. Shi, F. Wang, J. Tian, S. Li, E. Fu, J. Nie, R. Lei, Y. Ding, X. Chen, Z. L. Wang, *Sci. Adv.* **2021**, *7*, eabe2943.
- [24] H. Lei, J. Xiao, Y. Chen, J. Jiang, R. Xu, Z. Wen, B. Dong, X. Sun, *Nano Energy* **2022**, *91*, 106670.
- [25] H. Lei, K. Cao, Y. Chen, Z. Liang, Z. Wen, L. Jiang, X. Sun, *Chem. Eng. J.* **2022**, *445*, 136821.
- [26] J. Liu, Z. Wen, H. Lei, Z. Gao, X. Sun, *Nano-Micro Lett.* **2022**, *14*, 88.
- [27] H. Guo, X. Pu, J. Chen, Y. Meng, M.-H. Yeh, G. Liu, Q. Tang, B. Chen, D. Liu, S. Song, C. Wu, C. Hu, J. Wang, Z. L. Wang, *Sci. Rob.* **2018**, *3*, eaat2516.
- [28] C. Chen, Z. Wen, J. Shi, X. Jian, P. Li, J. T. W. Yeow, X. Sun, *Nat. Commun.* **2020**, *11*, 4143.
- [29] Y. Pang, X. Zhu, C. Lee, S. Liu, *Nano Energy* **2022**, *97*, 107219.
- [30] Q. Jing, Y. Xie, G. Zhu, R. P. Han, Z. L. Wang, *Nat. Commun.* **2015**, *6*, 8031.
- [31] Y. S. Zhou, G. Zhu, S. Niu, Y. Liu, P. Bai, Q. Jing, Z. L. Wang, *Adv. Mater.* **2014**, *26*, 1719.
- [32] C. Li, D. Liu, C. Xu, Z. Wang, S. Shu, Z. Sun, W. Tang, Z. L. Wang, *Nat. Commun.* **2021**, *12*, 2950.
- [33] Z. Wang, J. An, J. Nie, J. Luo, J. Shao, T. Jiang, B. Chen, W. Tang, Z. L. Wang, *Adv. Mater.* **2020**, *32*, 2001466.
- [34] Y. K. Pang, X. H. Li, M. X. Chen, C. B. Han, C. Zhang, Z. L. Wang, *ACS Appl. Mater. Interfaces* **2015**, *7*, 19076.
- [35] Z. Wu, W. Ding, Y. Dai, K. Dong, C. Wu, L. Zhang, Z. Lin, J. Cheng, Z. L. Wang, *ACS Nano* **2018**, *12*, 5726.
- [36] B. Zhang, Z. Wu, Z. Lin, H. Guo, F. Chun, W. Yang, Z. L. Wang, *Mater. Today* **2021**, *43*, 37.
- [37] H. Zhang, D. Ma, S. V. Raman, *SAE Trans.* **2004**, *113*, 488.
- [38] R. Zhang, H. Olin, *EcoMat* **2020**, *2*, e12062.
- [39] S. Niu, Y. Liu, S. Wang, L. Lin, Y. S. Zhou, Y. Hu, Z. L. Wang, *Adv. Mater.* **2013**, *25*, 6184.